Chinese Chemical Letters 36 (2025) 110204

Contents lists available at ScienceDirect

Chinese Chemical Letters

journal homepage: www.elsevier.com/locate/cclet

Cross-section design of the flow channels in membrane electrode assembly electrolyzer for CO_2 reduction reaction through numerical simulations

Lili Zhang[a,b], Hui Gao[a,b], Gong Zhang[a,b], Yuning Dong[a,b,e], Kai Huang[a,b], Zifan Pang[a,b], Tuo Wang[a,b,c], Chunlei Pei[a,b,c,*], Peng Zhang[a,b,c,e,*], Jinlong Gong[a,b,c,d]

[a] Key Laboratory for Green Chemical Technology of Ministry of Education, School of Chemical Engineering and Technology, Tianjin University, Tianjin 300072, China
[b] Collaborative Innovation Center of Chemical Science and Engineering (Tianjin), Tianjin 300072, China
[c] Haihe Laboratory of Sustainable Chemical Transformations, Tianjin 300192, China
[d] National Industry-Education Platform of Energy Storage, Tianjin University, Tianjin 300350, China
[e] Joint School of National University of Singapore and Tianjin University, International Campus of Tianjin University, Fuzhou 350207, China

ARTICLE INFO

Article history:
Received 10 April 2024
Revised 30 June 2024
Accepted 2 July 2024
Available online 6 July 2024

Keywords:
Electrochemical reduction of CO_2
Membrane electrode assembly
Mass transfer
Gas diffusion electrode
Computational fluid dynamics

ABSTRACT

Membrane electrode assembly (MEA) is widely considered to be the most promising type of electrolyzer for the practical application of electrochemical CO_2 reduction reaction (CO_2RR). In MEAs, a square-shaped cross-section in the flow channel is normally adopted, the configuration optimization of which could potentially enhance the performance of the electrolyzer. This paper describes the numerical simulation study on the impact of the flow-channel cross-section shapes in the MEA electrolyzer for CO_2RR. The results show that wide flow channels with low heights are beneficial to the CO_2RR by providing a uniform flow field of CO_2, especially at high current densities. Moreover, the larger the electrolyzer, the more significant the effect is. This study provides a theoretical basis for the design of high-performance MEA electrolyzers for CO_2RR.

The electrochemical CO_2 reduction reaction (CO_2RR) converts CO_2 into value-added products under mild conditions, with renewable electricity (*e.g.*, from wind and solar) as the potential energy supply [1-4]. In recent years, apparent progress has been achieved in the development of active electrocatalysts for CO_2RR [5-11]. Meanwhile, the design of suitable electrolyzers for the industrialization of the technique is still under investigation. Specifically, H-cells are used because of the low cost and ease of operation, which are useful for screening electrocatalysts and intrinsic kinetic studies [12]. However, the solubility of CO_2 in aqueous electrolytes is low, resulting in limited operating current densities [1]. Techno-economic analysis highlights the need to run CO_2RR at current densities above 100 mA/cm^2 to achieve industrial viability [13]. Therefore, gas diffusion electrodes (GDEs), which can provide a thin diffusion boundary layer that helps overcome the CO_2 mass transfer limitations in aqueous systems [14-16], are widely used in combination with flow cells [17,18]. To further lower the cell voltage and promote the energy conversion efficiency in flow cells [12], membrane electrode assembly (MEA) with a zero-gap configuration, similar to that used in fuel cells, has been adopted as the most promising electrolyzer for the practical application of CO_2RR [19,20].

Although MEAs use GDEs to overcome the solubility problem of CO_2 for achieving high current densities, the uneven CO_2 concentration throughout the entire flow channel with the proceeding of the reaction would affect the functioning of the active sites, especially for those close to the outlet of the reactor [21]. This problem is hard to be solved by the optimization of the catalyst. Regulation of the flow field to enhance the mass transfer of CO_2 within the flow channel, letting it reach the active sites more easily, would be an effective solution [22]. However, the complex mass transfer processes and the zero-gap configuration of MEA make it challenging to experimentally verify the local environments in the GDEs. Therefore, various studies have focused on numerical simulation using computational fluid dynamics (CFD) to understand the mass transfer on porous GDEs, and the mass diffusion-convection caused

* Corresponding authors.
E-mail addresses: chunlei.pei@tju.edu.cn (C. Pei), p_zhang@tju.edu.cn (P. Zhang).

https://doi.org/10.1016/j.cclet.2024.110204
1001-8417/

by complex flow patterns. CFD simulations could provide important data that could hardly be obtained through conventional experiments. It could also be performed at a low cost in a short time. However, it is difficult to take all the experimental conditions into account when using CFD simulation for research, and some simplifications are needed that may cause variations between the simulation results and the real-world scenarios.

The application of CFD modelling to guide the promotion of mass transfer in MEAs is developing fast [23-28]. Zhang *et al.* developed a comprehensive three-dimensional (3D) multiphase model of a proton exchange membrane fuel cell (PEMFC) and demonstrated that the addition of baffles in the cathode channel could increase the oxygen concentration in the porous electrode and promote water removal. These effects can effectively prevent the concentration loss in the flow channels of PEMFC [29]. Bao *et al*. investigated the two-phase flow in a 3D fine-mesh flow field using the volume of fluid (VOF) method. They found the air-guided effect of the 3D baffle enhanced the transport of reactants. In addition, there are some studies based on mass transfer and water management, the design of new flow channels to facilitate mass transfer [30,31]. Although these studies revealed the importance of reactant diffusion, their designs for fuel cells cannot be directly applied to CO_2RR. Therefore, the diffusion of gas-phase CO_2 to the catalyst surface should be carefully considered and new methods to enhance the CO_2 reduction reaction need to be proposed.

Recently, Weng *et al*. developed a multiphysics model of a GDE for CO_2RR, which is used to study the interactions between species transport and electrochemical reaction kinetics [32]. Kas *et al*. developed a two-dimensional transport model for a GDE that performs CO_2 reduction to CO. This model predicts that both CO_2 and buffer electrolyte concentrations decrease gradually along the channel due to electrochemical conversion and non-electrochemical depletion in the presence of parallel gas and electrolyte flow [21]. These computational studies have provided meaningful insights for improving the mass transfer of reactants during CO_2RR. However, further studies with the considerations of the geometric effect and the transport in multiple dimensions, especially for large MEA electrolyzers, are still urgently needed. For instance, the shape of the flow channel cross-section is one of the key factors to influence the transport processes. Different cross-section shapes with varied channel heights and widths affect the velocity and pressure of the gas in the flow channel, thus determining the concentration of CO_2 reaching the gas diffusion layer and the overall performance of the electrolyzer. Considering this point, we conducted numerical simulations of the CO_2RR coupled with mass transfer processes in MEA electrolyzers with rectangular, triangular, trapezoidal, semicircular, and dovetail flow channels. The impact of the cross-section shape of the channels on the distribution of CO_2 concentration and the electrolyzer performance was investigated. The results indicate that wide flow channels with lower heights can provide a uniform flow of CO_2, particularly at high current densities, thereby benefiting CO_2RR. Additionally, the larger the geometric dimensions of the electrolyzer, the more apparent this effect becomes.

A three-dimensional isothermal steady-state model was developed as the cathode of an MEA electrolyzer for CO_2RR (Fig. S1 in Supporting information). The computational domain includes the cathode flow field in the channel, gas diffusion layer, and catalyst layer. The detailed mesh of the model is shown in Fig. S1a. The number of grid cells for the rectangular flow channel model is 97,427, the minimum mesh is 0.12, and the average mesh element quality is 0.66. Five different cross-section shapes of the flow channels are selected namely rectangle, triangle, trapezoid, dovetail, and semicircle. Grid elements with other cross-section shapes are shown in the supporting information (Figs. S2-S5 in Supporting information).

In this model, the gas diffusion layer is assumed to be isotropic [33]. The length of the gas diffusion layer (L_{GDL}) is 315 μm [34,35]. The catalyst layer consists of spherical Ag nanoparticles with the radius of r_{np} that are loosely bound by a binder with the substrate possessing an intrinsic porosity of ε_{CL}^{O}. The solid volume fraction is $1-\varepsilon_{CL}^{O}$. The volume fractions of liquid and gas are $\varepsilon_{CL}^{O}S$ and $\varepsilon_{CL}^{O}(1-S)$, where S represents the catalyst layer saturation [32,33]. The MEA electrolyzer is assumed to operate at a steady state with gaseous mixtures are incompressible ideal gas in laminar flow. The effect of gravity is ignored [32-34].

The characteristic dimensions, airflow velocity, and pressure of the CO_2RR electrolyzer determine the flow state of the gas, thus requiring the selection of the appropriate control equation. Two charge transfer reactions are assumed to occur in the catalyst layer: the CO_2RR (Eq. 1) and the H_2 evolution reaction (Eq. 2) in alkaline environment [18].

$$CO_2 + H_2O + 2e^- \rightarrow CO + 2OH^- \quad (1)$$

$$2H_2O + 2e^- \rightarrow H_2 + 2OH^- \quad (2)$$

The mass balance of each species in the flow channel, gas diffusion layer and catalyst layer can be written as follows (Eq. 3):

$$\nabla \cdot n_i = R_{CT,i} \quad (3)$$

where n_i is the mass flux, $R_{CT,i}$ are the bulk charge transfer reactions [32]. $R_{CT,i}$ are applied to both gas and liquid phase species.

The gaseous species fluxes include a diffusion term and a convection term (Eq. 4),

$$n_i = j_i + \rho_i u_g \quad (4)$$

where j_i is the diffusion mass flux of species i, ρ_i is the mass density of species i, u_g is the mass-averaged fluid flow rate [32]. The diffusion fluxes were calculated using a mixture averaged diffusion model [34], the equation is formulated as follows (Eq. 5):

$$j_i = -\rho_g D_i^{eff} \nabla \omega_i - \rho_g D_i^{eff} \omega_i \frac{\nabla M_n}{M_n} \quad (5)$$

where ω_i is the mass fraction of species i, ρ_g is the density of the gaseous mixture, M_n is the average molar mass of the mixture (Eq. 6) [32].

$$M_n = \left(\sum_i \frac{\omega_i}{M_i} \right)^{-1} \quad (6)$$

D_i^{eff} is the effective diffusion coefficient of species i. The diffusion coefficient consists of the mass-averaged Stefan-Maxwell diffusivity and the Knudsen diffusivity (Eq. 7) [34], The formula for calculating the mass-averaged Stefan-Maxwell diffusivity (Eq. 8) and the Knudsen diffusivity (Eq. 9) is shown below:

$$D_i = \left(\frac{1}{D_i^m} + \frac{1}{D_i^K} \right)^{-1} \quad (7)$$

$$D_i^m = \frac{1-\omega_i}{\sum_{n \neq i} \frac{y_n}{D_{in}}} \quad (8)$$

$$D_i^K = \frac{2 r_{p,m}}{3} \sqrt{\frac{8RT}{\pi M_i}} \quad (9)$$

$r_{p,m}$ is the average pore radius of porous media, y_i and M_i are the molar fraction and molar mass of substance i, respectively. The binary gas-phase diffusion coefficients, D_{in}, are estimated following

derivation by Fuller *et al.* [36], the calculation formula is as follows (Eq. 10):

$$D_{in}\left[\mathrm{cm^2 s^{-1}}\right]=\frac{10^{-3}T[\mathrm{K}]^{1.75}\left(M_i\left[\mathrm{g\ mol^{-1}}\right]^{-1}+M_q\left[\mathrm{g\ mol^{-1}}\right]^{-1}\right)^{0.5}}{p[\mathrm{atm}]\left({\nu_{p,i}}^{0.33}+{\nu_{p,q}}^{0.33}\right)^2} \tag{10}$$

where $\nu_{p,i}$ is the special diffusion parameter to be summed over atoms, groups, and structural features of the diffusing species.

In addition, for flow through porous media (catalyst layer and gas diffusion layer), the effective diffusivity is corrected according to the porosity (ε_m) and tortuosity (τ_m) of the media, using the Bruggeman relation (Eq. 11) [32-34],

$$D_i^{\mathrm{eff}} = \frac{\varepsilon_\mathrm{m}}{\tau_\mathrm{m}}D_i = {\varepsilon_\mathrm{m}}^{3/2}D_i \tag{11}$$

where ε_m is the porosity of the porous medium.

To describe the mass-averaged velocity field in porous media, u_g, Darcy's law is used (Eq. 12),

$$u_g = -\frac{\kappa_\mathrm{m}^{\mathrm{eff}}}{\mu_g}\nabla p_G \tag{12}$$

where $\kappa_\mathrm{m}^{\mathrm{eff}}$ is the effective permeability of the porous medium, μ_g is the fluid viscosity, and p_G is the total gas pressure [33]. The calculation method for effective permeability is calculated as follows (Eq. 13):

$$\kappa_\mathrm{m}^{\mathrm{eff}} = \kappa_{\mathrm{sat,m}}\kappa_{\mathrm{r,m}} \tag{13}$$

$\kappa_{\mathrm{sat,m}}$ is the saturated permeability, $\kappa_{\mathrm{r,m}}$ is the relative permeability. $\kappa_{\mathrm{sat,m}}$ is determined by the structure of the medium, according to Carman–Kozeny equation (Eq. 14) [37].

$$\kappa_{\mathrm{sat,m}} = \kappa_{\mathrm{sat,m}}^{\mathrm{o}}\frac{{\varepsilon_\mathrm{m}}^3}{(1-\varepsilon_\mathrm{m})^2} \tag{14}$$

The values of $\kappa_{\mathrm{sat,m}}^{\mathrm{o}}$ are given in Table 1. Relative permeability (Eq. 15) is assumed to be cubically related to saturation [38], and therefore

$$\kappa_{\mathrm{r,m}} = (1-S)^3 \tag{15}$$

The fraction of the Nth gaseous species is determined by (Eq. 16)

$$\sum_i \omega_i = 1 \tag{16}$$

The conservation of charge (Eq. 17) and Ohm's law (Eq. 18) govern the electron potential ϕ_s and the current i_s.

$$\nabla\cdot i_\mathrm{s} = -\nabla\cdot i_\mathrm{l} = -a_\mathrm{v}\sum_k i_k \tag{17}$$

$$i_\mathrm{s} = -\sigma_{\mathrm{s,m}}^{\mathrm{eff}}\nabla\phi_\mathrm{s} \tag{18}$$

Table 1
Simulation settings and parameters.

Parameter	Value	Unit	Ref.
T	293.15	K	Experimental value
P	1	atm	Experimental value
q_1	50	mL/min	Experimental value
L_{GDL}	315	μm	[35]
$\varepsilon_{\mathrm{GDL}}$	0.8		Experimental value
σ_{GDL}	220	S/m	[35]
$\kappa_{\mathrm{sat,m}}^{\mathrm{o}}$	1.34×10^{-12}	$\mathrm{m^2}$	[35]
$\nu_{\mathrm{p,H_2}}$	7.07		[36]
$\nu_{\mathrm{p,H_2O}}$	12.7		[36]
$\nu_{\mathrm{p,CO}}$	18.9		[36]
$\nu_{\mathrm{p,CO_2}}$	26.9		[36]

i_s is the current density in the solid phase. i_l is the current density in the liquid phase. i_k is the local partial current density of the reaction k. a_v is the active surface area defined in the following (Eq. 19). $\sigma_{\mathrm{s,m}}^{\mathrm{eff}}$ is the effective conductivity of the solid material in the medium, corrected by the Bruggeman relation (Eq. 11).

$$a_\mathrm{v} = \frac{3(1-\varepsilon_\mathrm{m})}{r_{\mathrm{np}}} \tag{19}$$

Charge transfer reactions (Eq. 20) occur at the electrode/electrolyte interface [33].

$$R_{\mathrm{CT},i} = \frac{\nu_i i_{\mathrm{loc}}}{nF} \tag{20}$$

F is Faraday's constant. n is the number of electrons transferred, and ν_i is the stoichiometric coefficient of species i (negative for reactants, positive for products). i_{loc} is the local current density of electrochemical reactions. The current density of the electrode reaction at the electrochemical interface is defined by means of a custom current density value.

Regarding the coupled theory of mass transfer and electrochemical reactions, the general chemical reaction equation (Eq. 21) when linking the species flux at the electrode surface to the current is as follows.

$$\sum_{\mathrm{ox}}\nu_{\mathrm{ox}}Ox + ne^- \rightleftharpoons \sum_{\mathrm{red}}\nu_{\mathrm{red}}Red \tag{21}$$

Ox denotes oxides and *Red* denotes reducing substances.

The inlet flux is 50 sccm, and the outlet boundary of the flow channel is a pressure condition, which inhibits reflux. The boundaries are flux-free conditions except for the inlet, outlet and electrochemical reaction interface.

It is assumed that the CO_2 in the feed is wet and the water vapor is saturated [33]. The saturated water vapor pressure is calculated as below (Eq. 22) [33,39].

$$p_{vap} = 10^{8.071\ -\ \frac{1730.63}{T[\mathrm{K}]\ -\ 39.724}}(\mathrm{mmHg}) \tag{22}$$

The formula for calculating the mass fraction of water is as follows (Eq. 23):

$$\omega_{\mathrm{H_2O}} = \frac{\frac{p_{vap}}{P}\times M_{\mathrm{H_2O}}}{\frac{p_{vap}}{P}\times M_{\mathrm{H_2O}} + \left(1-\frac{p_{vap}}{P}\right)\times M_{\mathrm{CO_2}}} \tag{23}$$

According to Eq. 16, the mass fraction of CO_2 ($\omega_{\mathrm{co_2}}$) can be obtained.

During the reaction in the MEA electrolyzer, the reactants CO_2 and H_2O reach the catalyst layer through the gas diffusion layer to participate in the reaction. The products CO and H_2 are generated in the cathode catalyst layer, which are discharged from the cell through the gas diffusion layer and the flow channel by gas diffusion and purging. As discussed above, the uniform distribution of CO_2 through the channel is essential to achieving high activity. According to the simulation model with the five different channel designs (Fig. S6 in Supporting information), the performance is evaluated by observing the concentration changes of the reactants on the contact surface between the flow channel and the gas diffusion layer.

When the areas of the five different cross-sections of flow channels are the same (Fig. S6a and Table 2), the CO_2 concentration distributions at the interface between the flow channel and the gas diffusion layer are shown in Fig. 1a. The left side is the inlet and the right side is the outlet (applicable for all the simulations conducted in this work). When the simulation is steady, the CO_2 concentration becomes smaller in the direction parallel to the flow channel, from the inlet to the outlet with the proceeding of the reaction. The CO_2 concentration distribution at the outlet section of the flow channel is shown in Fig. S7a (Supporting information). A certain concentration difference can be observed between

Table 2
Geometric parameters of the five different cross-sections of the flow channels with the same area.

Cross-section shape	L (mm)	C_W (mm)	C_H (mm)	A_{CS} (mm^2)	$A_{C\text{-}GDL}$ (mm^2)
Rectangle	20.00	1.00	1.00	1.00	20.00
Triangle	20.00	1.50	1.33	1.00	30.00
Trapezoid	20.00	1.50	1.00	1.00	30.00
Semicircle	20.00	1.60	0.80	1.00	31.90
Dovetail	20.00	0.50	1.00	1.00	10.00

L: channel length, C_W: channel width, C_H: channel height, A_{CS}: cross-section area of the flow channel, $A_{C\text{-}GDL}$: contact area between the flow channel and the gas diffusion layer.

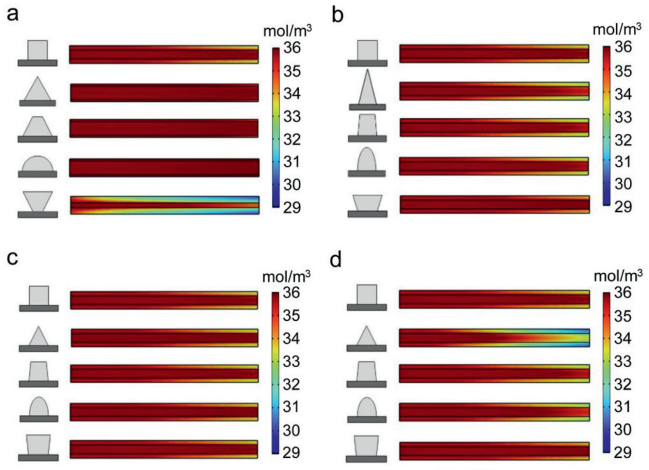

Fig. 1. CO_2 distributions at the interface between the flow channel and the gas diffusion layer. (a) The five different flow channels with the same cross-section areas. (b) The five different flow channels with the same cross-section area and the same channel width. (c, d) The five different flow channel cross-sections with the same channel width and channel height, but different areas. The gas flow rate at the inlet is the same for a-c. The gas flow velocity at the inlet is the same for d. The shape of the flow channel cross-section is rectangular, triangular, trapezoidal, semicircular, and dovetail. The left side is the inlet and the right side is the outlet.

the channel and the rib. The uniformity of gas concentration distribution is good for channels with triangle, trapezoid, and semicircle shapes. The semicircular flow channel has the most uniform gas concentration distribution. However, the rectangular and dovetail channels have uneven distributions of the reactant. It is worth noting that the uniformity of the CO_2 concentration has a close relationship with the width of the channel (Table 2). The wider the channel is, the better the CO_2 is distributed.

In addition to the apparent impact of the width of the channel, the height of the channel may also be important. The effect of channel height on gas distribution was investigated with models possessing the same channel cross-section area and channel width (Fig. S6b and Fig. 1b). The CO_2 concentration distribution at the outlet section of the flow channel is shown in Fig. S7b (Supporting information). Compared with the rectangular flow channel, the uniformity of the gas concentration distribution is promoted for the dovetail model, while it becomes worse for the triangular, trapezoidal, and semicircular shapes. The main reason for such change lies in the different channel heights of the flow channel cross sections (Table S1 in Supporting information). The smaller the channel height, the more uniform the gas concentration distribution at the contact interface between the channel and the gas diffusion layer.

According to the study above, both the channel width and channel height could influence the uniformity of CO_2 gas concentration distribution. Further investigation about the effect of channel shape on the uniformity of CO_2 distribution was conducted by ensuring the same channel width and channel height (Fig. S6c and Fig. 1c). The CO_2 concentration distribution at the outlet section of the flow channel is shown in Fig. S7c (Supporting information). It can be observed that the uniformity of CO_2 distribution for the five different shapes of the cross sections does not differ much under the same flow rate. Among them, the uniformity of concentration distribution of triangular and trapezoidal channels is slightly better than that of the rectangular one. The uniformity of gas concentration distribution of the semicircular and dovetail channels is slightly worse than that of the rectangular channel, but the difference is not significant. Therefore, it can be concluded that channel width and channel height are essential to affect the distribution of CO_2 during the reaction at a constant flow rate. Wide and low channels are beneficial for the uniform distribution of the reactant. In wide channels, the area for direct contact between CO_2 and the gas diffusion layer is large, which could be good for the dispersion of the reactant. When the channel height is small, the diffusion distance of the gas in the direction perpendicular to the flow channel is short, which could further lead to a more uniform CO_2 concentration distribution.

As discussed above, the impact of the channel shape is not significant when the width and the height of the channel are fixed with a constant flow rate of CO_2. To further search for the optimized cross-section shape of flow channels, simulations with a constant flow velocity were conducted for the five different channels (Fig. 1d). The CO_2 concentration distribution at the outlet section of the flow channel is shown in Fig. S7d (Supporting information). The triangular, trapezoidal, and semicircular channels have worse distribution of the reactant. Compared with the flow channel with the rectangular cross-section, the flow channel with the dovetail cross-section has better gas distribution uniformity. It is worth noting that the uniformity of the CO_2 distribution correlates with the cross-section areas of the channel (Table S2 in Supporting information). A larger channel cross-section area leads to a more uniform distribution. Therefore, the channels in a MEA electrolyzer for CO_2RR should better be wide and low with a large cross-section area.

To further verify the obtained design principle, whether similar trends could be achieved at different flow conditions was tested [21]. When the areas of the cross sections are the same (Fig. S6a), the trends of CO_2 concentration distributions for the five different cross-section shapes at flow rates of 10 sccm (Fig. 2a and Fig. S8a in Supporting information), 30 sccm (Fig. 2b and Fig. S8b in Sup-

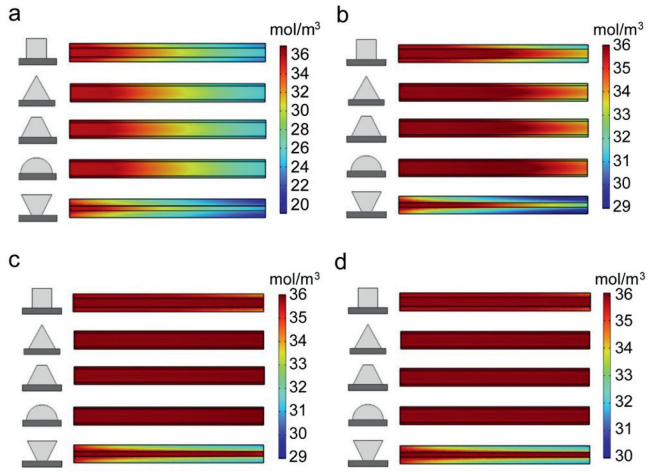

Fig. 2. CO_2 distributions at different flow rates: (a) 10 sccm, (b) 30 sccm, (c) 70 sccm, (d) 90 sccm. The shape of the flow channel cross-section is rectangular, triangular, trapezoidal, semicircular and dovetail. Flow channel designs are similar to those used in Fig. S6.

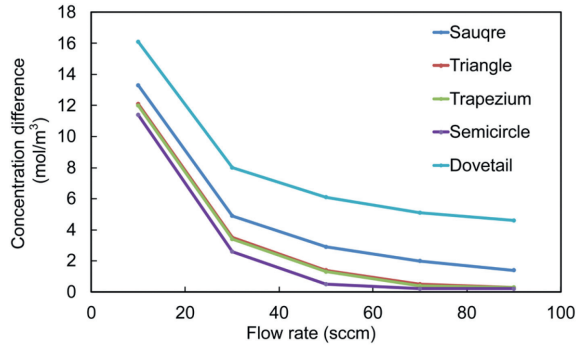

Fig. 3. Difference between the maximum and the minimum CO_2 concentrations at the contact interface between the flow channel and the gas diffusion layer at different flow conditions. The five different flow channels with the same cross-section area.

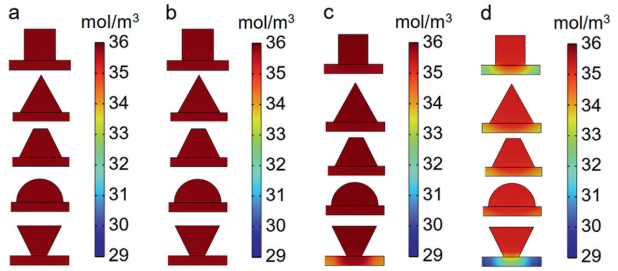

Fig. 4. CO_2 distributions at the flow channel exit interface at different current densities: (a) 100 mA/cm^2, (b) 200 mA/cm^2, (c) 600 mA/cm^2, (d) 1000 mA/cm^2. The shape of the flow channel cross-section is rectangular, triangular, trapezoidal, semicircular and dovetail. Flow channel designs are similar to those used in Fig. S6. The flow rate is a constant value of 50 sccm.

porting information), 70 sccm (Fig. 2c and Fig. S8c in Supporting information), and 90 sccm (Fig. 2d and Fig. S8d in Supporting information) were consistent with that at the flow rate of 50 sccm (Fig. 1a). In addition, the higher the flow rate, the better the distribution is (Fig. 2). Similar results could be obtained for other conditions when the channels with the same areas and widths are used or the channels with the same widths and heights are applied (Figs. S9-S12 in Supporting information).

The difference between the maximum CO_2 concentration and the minimum CO_2 concentration at the interface between the gas diffusion layer and the catalyst layer was calculated as an indicator of the uniformity of CO_2 (Fig. 3). As the flow rate increases, the CO_2 concentration difference becomes smaller. At low flow rates, such as 10 sccm and 30 sccm, an increase in flow rate increases the degree of uniformity. However, under high flow rate conditions, such as 70 sccm and 90 sccm, a further increase in flow rate has little impact on the degree of uniformity, when mass transfer is no longer a limiting factor. Although increasing the flow rate will improve uniformity, it will sacrifice the single-pass conversion of CO_2. When the cross-section area of the flow channel is the same, the concentration difference of the semicircular cross-section flow channel is the smallest, indicating a more uniform concentration distribution (Fig. 3), which is in consistence with the previous result (Fig. 1a). For the other cases, the trends of CO_2 distribution at different flow conditions also follow those of the results above (Figs. S13-S15 in Supporting information).

The CO_2 distributions at the contact interface between the flow channel and the gas diffusion layer were also calculated at different current densities (Fig. S16 in Supporting information). The CO_2 distributions at the flow channel exit interface were also calculated at different current densities (Fig. 4). At low current density, the CO_2 concentration distribution is relatively uniform, without apparent difference for different channel cross-section shapes. With the increase of current density, the CO_2 concentration distribution varies. These results indicate that mass transfer is not the main limiting factor at low current densities. Only when the current density is high, the uniformity of the CO_2 concentration distribution needs to be considered with the careful design of the channels in the MEA electrolyzer. It is worth noting that the design of the channels should also consider the manufacturing difficulties, especially for practical applications.

In this study, numerical simulations of CO_2RR MEA electrolyzers with rectangular, triangular, trapezoidal, semicircular, and dovetail flow channels were carried out using computational fluid dynamics. The effects of the cross-section dimensions on the uniformity of CO_2 concentration distribution were investigated. The results show that under the same flow rate condition, the larger the channel width and the smaller the channel height, the more uniform the CO_2 distribution. Under the same flow velocity condition with channels with the same width and height, large cross-section area is beneficial for the uniformity the CO_2 distribution. Besides, this effect is more significant at low flow rates and high current densities. This work provides theoretical guidance for the design of high-performance MEA electrolyzer for CO_2RR.

Declaration of competing interest

The authors declare that they have no known competing financial interests or personal relationships that could have appeared to influence the work reported in this paper.

CRediT authorship contribution statement

Lili Zhang: Writing – original draft, Methodology, Investigation. **Hui Gao:** Methodology. **Gong Zhang:** Investigation. **Yuning Dong:** Investigation. **Kai Huang:** Methodology, Investigation. **Zifan Pang:** Methodology, Investigation. **Tuo Wang:** Writing – review & editing, Supervision. **Chunlei Pei:** Writing – review & editing, Methodology. **Peng Zhang:** Writing – review & editing, Methodology, Investigation. **Jinlong Gong:** Writing – review & editing, Methodology, Investigation, Conceptualization.

Acknowledgments

We acknowledge the National Key R&D Program of China (No. 2021YFA1501503), the National Natural Science Foundation of China (Nos. 22250008, 22121004, 22108197), the Haihe Laboratory of Sustainable Chemical Transformations (No. CYZC202107), the Natural Science Foundation of Tianjin City (No. 21JCZXJC00060), the Program of Introducing Talents of Discipline to Universities (No. BP0618007) and the Xplorer Prize for financial support.

Supplementary materials

Supplementary material associated with this article can be found, in the online version, at doi:10.1016/j.cclet.2024.110204.

References

[1] B. Jung, S. Park, C. Lim, et al., Chem. Eng. J. 424 (2021) 130265.
[2] Y. Sun, S. Wang, D. Jiao, et al., Chin. Chem. Lett. 33 (2022) 3987–3992.
[3] H. Zhang, C. He, S. Han, et al., Chin. Chem. Lett. 33 (2022) 3641–3649.
[4] X. Zhao, B. Deng, H. Xie, et al., Chin. Chem. Lett. 35 (2024) 109139.
[5] Z. Sun, T. Ma, H. Tao, Q. Fan, B. Han, Chem 3 (2017) 560–587.
[6] Y.J. Sa, C.W. Lee, S.Y. Lee, et al., Chem. Soc. Rev. 49 (2020) 6632–6665.
[7] Y. Dong, M. Ma, Z. Jiao, et al., Chin. Chem. Lett. 35 (2024) 109049.
[8] L. Li, F. Chen, B. Zhao, Y. Yu, Chin. Chem. Lett. 35 (2024) 109240.
[9] K. Kim, W.H. Lee, J. Na, et al., J. Mater. Chem. A 8 (2020) 16943–16950.
[10] D. Voiry, H.S. Shin, K.P. Loh, M. Chhowalla, Nat. Rev. Chem. 2 (2018) 105.
[11] H. Yao, M.Y. Wang, C. Yue, et al., Trans. Tianjin Univ. 29 (2023) 254–274.
[12] W. Ma, X. He, W. Wang, et al., Chem. Soc. Rev. 50 (2021) 12897–12914.

[13] S. Verma, B. Kim, H.R.M. Jhong, S. Ma, P.J.A. Kenis, ChemSusChem 9 (2016) 1972–1979.
[14] T. Burdyny, W.A. Smith, Energy Environ. Sci. 12 (2019) 1442–1453.
[15] D. Higgins, C. Hahn, C. Xiang, T.F. Jaramillo, A.Z. Weber, ACS Energy Lett. 4 (2018) 317–324.
[16] T.N. Nguyen, C.T. Dinh, Chem. Soc. Rev. 49 (2020) 7488–7504.
[17] H. Kohjiro, S. Noriyuki, S. Tadayoshi, Stud. Surf. Sci. Catal. 114 (1998) 577–580.
[18] S. Verma, X. Lu, S. Ma, R.I. Masel, P.J.A. Kenis, Phys. Chem. Chem. Phys. 18 (2016) 7075–7084.
[19] J.C. Bui, C. Kim, A.J. King, et al., Acc. Chem. Res. 55 (2022) 484–494.
[20] J.A. Rabinowitz, M.W. Kanan, Nat. Commun. 11 (2020) 5231.
[21] R. Kas, A.G. Star, K. Yang, et al., ACS Sustain. Chem. Eng. 9 (2021) 1286–1296.
[22] D. Gao, W. Li, H. Wang, G. Wang, R. Cai, Trans. Tianjin Univ. 28 (2022) 245–264.
[23] J.D. Duhn, A.D. Jensen, S. Wedel, C. Wix, J. Power Sources 336 (2016) 261–271.
[24] V.K. Krastev, G. Falcucci, E. Jannelli, M. Minutillo, R. Cozzolino, Int. J. Hydrog. Energy 39 (2014) 21663–21672.
[25] Q. Zhang, B. Wang, Trans. Tianjin Univ. 29 (2023) 360–386.
[26] J. Macedo-Valencia, J.M. Sierra, S.J. Figueroa-Ramírez, S.E. Díaz, M. Meza, Int. J. Hydrog. Energy 41 (2016) 23425–23433.
[27] J. Park, X. Li, J. Power Sources 163 (2007) 853–863.
[28] S. Ye, Y. Hou, X. Li, K. Jiao, Q. Du, Trans. Tianjin Univ. 29 (2023) 1–13.
[29] G. Zhang, L. Fan, J. Sun, K. Jiao, Int. J. Heat Mass Transf. 115 (2017) 714–724.
[30] C. He, Q. Wen, F. Ning, et al., Adv. Funct. Mater. 34 (2024) 2401261.
[31] C. He, Q. Wen, F. Ning, et al., Adv. Sci. 10 (2023) 2302928.
[32] L.C. Weng, A.T. Bell, A.Z. Weber, Phys. Chem. Chem. Phys. 20 (2018) 16973–16984.
[33] L.C. Weng, A.T. Bell, A.Z. Weber, Energy Environ. Sci. 12 (2019) 1950–1968.
[34] L.C. Weng, A.T. Bell, A.Z. Weber, Energy Environ. Sci. 13 (2020) 3592–3606.
[35] A. El-kharouf, T.J. Mason, D.J.L. Brett, B.G. Pollet, J. Power Sources 218 (2012) 393–404.
[36] E.N. Fuller, P.D. Schetle, J.C. Giddings, Ind. Eng. Chem. 58 (1966) 18–27.
[37] P.C. Carman, Chem. Eng. Res. Des. 75 (1997) 532–548.
[38] W.A. Z, N. J, Chem. Rev. 104 (2004) 4679–4726.
[39] D.G. Wheeler, B.A.W. Mowbray, A. Reyes, et al., Energy Environ. Sci. 13 (2020) 5126–5134.